Analytical and numerical analysis of lensing effect for linear surface water waves through a square array of nearly touching rigid square cylinders

M. Farhat, S. Guenneau,* S. Enoch, and G. Tayeb
Institut Fresnel-CNRS (UMR 6133), University of Aix-Marseille, 13397 Marseille cedex 20, France

A. B. Movchan and N. V. Movchan
Department of Mathematical Sciences, University of Liverpool, Peach Street, Liverpool L69 3BX, United Kingdom
(Received 26 February 2007; published 21 April 2008)

This paper describes transport properties of linear water waves propagating within a square array of fixed square cylinders. The main focus is on achieving the conditions for all-angle-negative-refraction (AANR) thanks to anomalous dispersion in fluid-filled periodic structures. Of particular interest are two limit cases when either the edges or the vertices of the cylinders come close to touching. In the former case, the array can be approximated by a lattice of thin water channels (for which dispersion curves are given in closed form and thus frequencies at which AANR occurs) whereas in the latter case, the array behaves as a checkerboard with cells consisting either of water tanks or rigid cylinders (for which standing modes are given in closed form). The tools of choice for the present analysis are, on the one hand, the finite element method which solves numerically spectral problems in periodic media, and on the other hand, a two-scale asymptotic method which provides estimates of dispersion curves and associated eigenfields through a lattice approximation (namely thin water channels between rigid cylinders). Simple duality correspondences are found based on fourfold symmetry of square water checkerboards that allow us to get some insight into their spectra. Last, some numerical evidence is provided for water waves focusing with no astigmatism through such arrays, when they are of finite extent.

DOI: 10.1103/PhysRevE.77.046308 PACS number(s): 47.65.-d, 47.35.Lf, 47.11.Fg, 47.11.St

I. INTRODUCTION

Veselago, in 1967, postulated the existence of materials with simultaneously negative permittivity (ε) and magnetic permeability (μ) which were shown to have a negative refractive index [1]. In his visionary paper, Veselago also proposed to use negative refraction to make a convergent flat lens. Thirty years afterwards, in 2000, Pendry further showed it is possible to design a flat lens that overcomes the diffraction limit through enhancement of evanescent waves via plasmon resonances occurring on the boundaries of the slab lens when its refractive index is close to -1 [2,3]. Pendry's perfect lens can be generalized to checkerboard metamaterials satisfying a mirror antisymmetry [4]. The experimental demonstration of negative refractive index materials at GHz frequencies by Smith and co-workers in 2000 [5] fueled the research in the area of metamaterials which are structured at subwavelength length scales [6] (one can regard them as almost homogeneous). Using photonic crystals (PC) [7], a very similar negative refraction effect at all angles of incidence was independently predicted in [8–11]. Alike photonic crystals, negative refraction has been demonstrated in sonic crystals, also leading to lensing effects [12,14].

Recently, some progress has been made on theoretical analysis [15–19] of the band structures and the possibility of the existence of band gaps for liquid surface waves propagating in periodic structures. Among others, the multiple scattering method, which is particularly well suited for arrays of circular cylindrical bodies, the plane-wave method which tackles noncircular geometries and the variational method have been used. In [18], Torres *et al.* further investigated experimentally Floquet-Bloch water Rayleigh waves by visualizing the patterns of liquid surface waves propagating over a bottom with periodically drilled holes. Focusing effect was further investigated both theoretically and experimentally by Hu *et al.* [13] using a square array of circular cylindrical holes. But to our knowledge, nobody addressed the question of stop bands and super-focusing effects for water waves propagating in arrays of square cylinders with either edges or vertices nearly touching: These two limit cases correspond, respectively, to a lattice of thin intersecting water channels and a rigid checkerboard with one-half of its cells filled with water. In the former case, we are able to carry out analytical estimates for dispersion curves and most importantly for the working frequency of the liquid lens. In the latter case, standing modes are well approximated by analytical resonances of a square water tank.

II. GOVERNING EQUATIONS

A. Equations in a homogeneous medium

Let us denote by Ω the open bounded set in $\mathbb{R}^3$ within which lies the transverse components of the fluid. The conservation of momentum in inviscid fluids leads to so-called Euler's equations,

$$\frac{\partial \mathbf{u}}{\partial t} + (\mathbf{u}\cdot\nabla)\mathbf{u} + \frac{\nabla p}{\rho} = \mathbf{g} \quad \text{in } \Omega, \tag{1}$$

where $\mathbf{u}$ is the velocity field, p is the pressure, ρ is the fluid density, and $\mathbf{g}$ is the vector of gravity force, $\mathbf{g}=-g\mathbf{e}_3$, where g denotes the acceleration caused by gravity.

*sebastien.guenneau@fresnel.fr

We further assume that the fluid is incompressible and irrotational

$$\nabla \cdot \mathbf{u} = 0, \quad \nabla \times \mathbf{u} = \mathbf{0} \quad \text{in } \Omega. \tag{2}$$

There exists a velocity potential Φ such that

$$\mathbf{u} = \nabla \Phi \quad \text{in } \bar{\Omega}, \tag{3}$$

where $\bar{\Omega}$ stands for the fluid region Ω together with any fixed interface in contact with it (such as some water tank boundaries). We also have

$$\nabla^2 \Phi = 0 \quad \text{in } \Omega. \tag{4}$$

So far, the Laplace equation (4) does not manifest a wave character: Waves are induced by the boundary conditions on the free surface separating the liquid and air.

Let $x_3 = \xi(x_1, x_2, t)$ be the equation of the free surface. The pressure is prescribed to be equal to the constant atmospheric pressure p_0 on $x_3 = \xi(x_1, x_2, t)$, and the surface tension is neglected. Hence, (1) and (3) lead to Bernoulli's equation

$$\frac{\partial \Phi}{\partial t} + \frac{|\nabla \Phi|^2}{2} + \frac{p_0}{\rho} + g\xi = f(t) \quad \text{on } x_3 = \xi. \tag{5}$$

Assuming that $f(t)$ is incorporated into Φ and that liquid fluctuations are small, i.e., $|\xi - h| \ll 1$, where h denotes the mean value of ξ, and also $|\frac{\partial \xi}{\partial x_j}| \ll 1$, $j = 1, 2$, differentiation of (5) with respect to t leads to the linearized equation

$$\frac{\partial^2 \Phi}{\partial t^2} + g\frac{\partial \xi}{\partial t} = 0 \quad \text{on } x_3 = h. \tag{6}$$

Using the ansatz

$$u_3 = \frac{dx_3}{dt} = \frac{\partial \xi}{\partial t} + \frac{\partial \xi}{\partial x_1}\frac{\partial x_1}{\partial t} + \frac{\partial \xi}{\partial x_2}\frac{\partial x_2}{\partial t} \sim \frac{\partial \xi}{\partial t}, \tag{7}$$

Eqs. (3) and (6) lead to Poisson's condition

$$\frac{\partial^2 \Phi}{\partial t^2} + g\frac{\partial \Phi}{\partial x_3} = 0 \quad \text{on } x_3 = h. \tag{8}$$

Altogether, Φ is the solution of the following system [20,21]:

$$\nabla^2 \Phi = 0 \quad \text{for } x_3 \in]0, h[,$$

$$\frac{\partial^2 \Phi}{\partial t^2} + g\frac{\partial \Phi}{\partial x_3} = 0 \quad \text{for } x_3 = h,$$

$$\mathbf{n} \cdot \nabla \Phi = 0 \quad \text{for } x_3 = 0, \tag{9}$$

where the last boundary condition accounts for a no-flow condition through the plane $x_3 = 0$ (this stands for the fixed surface at the bottom of the water tank).

B. Dispersion relation in a liquid without inclusions

If we look for solutions of (9) in the form

$$\Phi(x_1, x_2, x_3, t) = f(x_3) e^{-i(wt - \kappa_1 x_1 - \kappa_2 x_2)}, \tag{10}$$

Laplace's equation leads to

$$f''(x_3) - \kappa^2 f(x_3) = 0, \tag{11}$$

with $\kappa = \sqrt{\kappa_1^2 + \kappa_2^2}$. Hence, the Neumann boundary condition in (9) gives

$$f(x_3) = A \cosh(\kappa x_3). \tag{12}$$

Using now the boundary condition at $x_3 = h$, we obtain the dispersion relation

$$\omega^2 = g\kappa \tanh(\kappa h). \tag{13}$$

For the applications discussed later in this paper, this equation should be refined to take into account the capillarity through the existence of the surface tension σ. Indeed, the pressure of the surface of the liquid is equal to $p_0' = p_0 - \sigma \nabla^2 \xi$, where $\frac{\partial^2 \xi}{\partial x_j^2}$, $j = 1, 2$, accounts for the curvature of the liquid surface.

In this case, Poisson's condition (8) becomes

$$\frac{\partial^2 \Phi}{\partial t^2} + g\frac{\partial \Phi}{\partial x_3} - \frac{\sigma}{\rho}\frac{\partial \nabla^2 \Phi}{\partial x_3} = 0, \tag{14}$$

so that the dispersion relation is reexpressed as

$$\omega^2 = \left(g + \frac{\sigma}{\rho}\kappa^2\right)\kappa \tanh(\kappa h). \tag{15}$$

In the literature, Eq. (15) is sometimes written $\omega^2 = g\kappa(1 + d_c^2)\tanh(\kappa h)$, where $d_c = \kappa\sqrt{\sigma/(\rho g)}$ is the capillarity.

C. Helmholtz equation on a free surface for the reduced potential

We can now look for solutions in terms of the reduced potential ϕ,

$$\Phi(x_1, x_2, x_3, t) = \mathrm{Re}[\phi(x_1, x_2)\cosh(\kappa x_3) e^{-i\omega t}], \tag{16}$$

which leads us to the Helmholtz equation

$$\nabla^2 \phi + \kappa^2 \phi = 0, \tag{17}$$

where κ is the spectral parameter linked to the wave frequency through the dispersion relation (15).

Finally, the vertical displacement of the liquid surface ξ is related to the potential ϕ by

$$\xi(x_1, x_2, t) = \mathrm{Re}\left(-\frac{i\omega}{g}\phi(x_1, x_2) e^{-i\omega t}\right). \tag{18}$$

D. Neumann boundary conditions on rigid cylindrical inclusions immersed into the fluid

In the sequel we shall consider immersed bodies within the fluid. Hence Ω is not simply connected and (2) does not necessarily imply (3): There may be additional so-called cohomology terms in the potential Φ. To avoid that, the so-called no-flow condition should be taken into account on the boundaries between fluid and structure: Let $s(x_1, x_2, t) = 0$ be the equation describing the boundary S of each immersed body, then

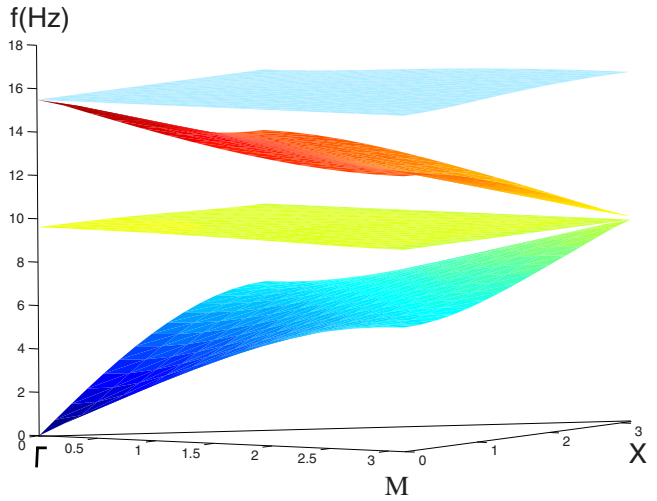

FIG. 1. (Color online) Finite element method (FEM) computations of dispersion surfaces associated with water waves propagating within a square array of pitch 10 mm consisting of fixed square cylinders of side length 0.9487 mm immersed in water (the filling fraction of cylinder in water $F=0.9$). Horizontal axes: Components k_1 and k_2 of the Bloch vector describing the area of the first Brillouin zone ΓXM. Vertical axis: Wave frequency $f=\omega/(2\pi)$ in Hz. The depth of water is $h=6$ mm and the capillarity $d_c=0.109$ mm.

$$\frac{ds}{dt} = \mathbf{u}\cdot\nabla s + \frac{\partial s}{\partial t} \quad \text{on } S. \tag{19}$$

This expresses the kinematic property that there is no transfer of matter across the boundary.

Taking into account (3), the no-flow condition (19) leads to

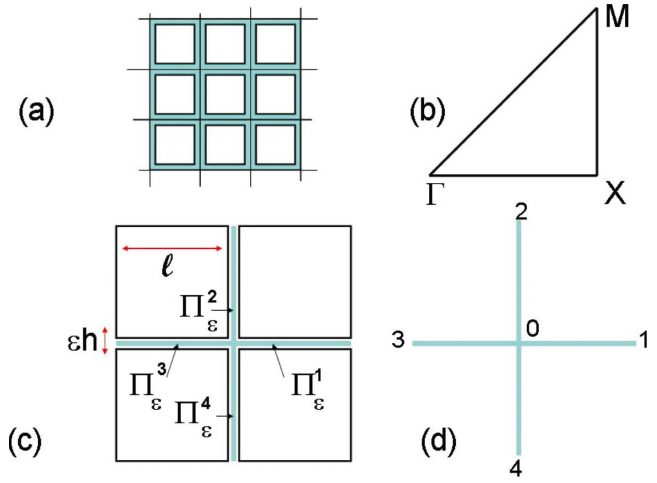

FIG. 2. (Color online) (a) Square array of square cylinders of pitch 1 where the blue region is filled with water; (b) corresponding reduced Brillouin zone ΓXM where $\Gamma=(0,0)$, $X=(0,\pi)$, and $M=(\pi,\pi)$; (c) selected region of the square array showing four square cylinders separated by four thin bridges Π_ε^j of thickness εh, $\varepsilon \ll 1$, and length l, within which water flows (blue region). (d) Corresponding lattice structure with a central node 0 and four nodes $1,\ldots,4$ at which the potential takes the values Φ_j, $j=0,\ldots,4$ satisfying the boundary conditions (38) and (39).

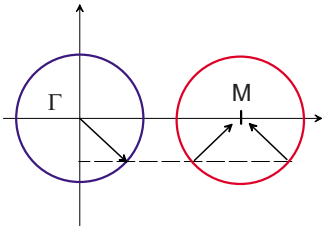

FIG. 3. (Color online) Schematic representation of the EFS for the water waves propagating freely (left-hand circle) and the Bloch waves in the crystal (right-hand circle). The dashed line shows the conservation of the tangential component of the wave vector.

$$\frac{\partial\Phi}{\partial n} = -\frac{1}{|\nabla s|}\frac{\partial s}{\partial t} = u_n \quad \text{on } S, \tag{20}$$

where u_n denotes the normal component of the velocity field $\mathbf{u}$. This means that the normal velocity of particles is continuous across a physical boundary.

If S is a fixed (rigid) interface, (20) simplifies to

$$\frac{\partial\Phi}{\partial n} = 0 \quad \text{on } S, \tag{21}$$

which is a natural boundary condition (homogeneous Neumann boundary condition).

E. Floquet-Bloch water waves

Let ϕ be functions of spatial variables of finite energy in $Y=[0;1]^2$ (square integrable and with a square integrable gradient) and such that

$$\phi(x_1+1,x_2+1) = \phi(x_1,x_2)e^{i(k_1+k_2)}, \tag{22}$$

where the Bloch vector $\mathbf{k}=(k_1,k_2)\in Y^*=[0,\pi]^2$, where Y^* is the so-called first Brillouin zone. (See Figs. 1–4.) This square cell Y^* in reciprocal space can be further reduced to a

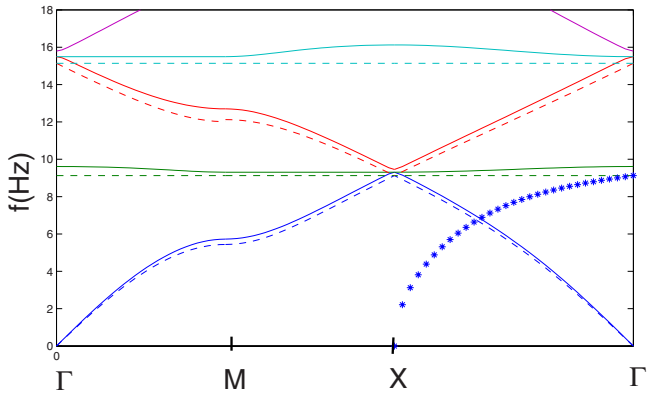

FIG. 4. (Color online) Comparison of FEM computations of dispersion curves (continuous curves) against analytical estimate (41) (dotted curves) for a filling fraction of cylinder in water of 0.9. Horizontal axis: Projection of the Bloch vector on the first Brillouin zone ΓXM. Vertical axis: Wave frequency $f=\omega/(2\pi)$ in Hz. The starred curve corresponds to surface waves propagating in water along the ΓM direction, as given by Eq. (15). The depth of water is $h=6$ mm and the capillarity $d_c=0.109$ mm.

square triangle ΓMX with vertices $\Gamma=(0,0)$, $M=(0,\pi)$, and $X=(\pi,\pi)$, as depicted in Fig. 2(b) if the inclusion within the cell Y in physical space exhibits a fourfold symmetry.

F. Variational formulation and well-posedness

Multiplying (17) by a smooth test function ψ and using Green's formula and (21), we obtain the weak form of the water-wave equation,

$$-\int_Y \nabla\phi\cdot\nabla\psi \; dx_1dx_2+\kappa^2\int_Y \phi\psi \; dx_1dx_2=0. \qquad (23)$$

This expression is then discretized using test functions ψ taking values on nodes of a triangular mesh of the basic cell Y. To enforce Floquet-Bloch conditions in (23), it is enough to link values of V on opposite sides of the basic cell Y (see [22] for electromagnetic waves). The finite element formulation was implemented in the commercial package COMSOL multiphysics [23].

The resolvent of the operator associated with the quadratic form (23) is compact, hence for a given Bloch vector $\mathbf{k}$ the spectrum is a countable set of isolated eigenvalues tending to infinity that can be ordered by increasing number $\kappa_n(\mathbf{k})$ (with the integer n taking into account the multiplicity of a given eigenvalue κ_n). More precisely, these eigenvalues can be numerically found using the Rayleigh quotient form of (23) and invoking the Courant-Fischer min-max principle [24] which says that for all $n\geq 1$, one has

$$\kappa_n^2(\mathbf{k})=\min_{U_{n-1}\in H_{n-1}}\max_{0\neq\phi\in U_{n-1}^{\perp}}\frac{\displaystyle\int_Y|\nabla\phi|^2dx_1dx_2}{\displaystyle\int_Y|\phi|^2dx_1dx_2}, \qquad (24)$$

where H_n is the set of subspaces of dimension n of the infinite-dimensional Hilbert space $H_\sharp(\mathbf{k},Y)=\{(\phi,\nabla\phi)\in L^2(Y)\times[L^2(Y)]^2,\ \phi$ satisfies (22)$\}$. The larger n, the finer the approximation of $H_\sharp(\mathbf{k},Y)$ by H_n (density result). The numerical counterpart is nothing but the iterative Lanczos algorithm which is well suited for large sparse matrices appearing in finite element methods (FEM) [22].

Now, each eigenvalue depends smoothly upon the Bloch parameter $\mathbf{k}$, so that when $\mathbf{k}$ describes the Brillouin zone, we end up with a band spectrum

$$\sigma_{\text{Bloch}}=\bigcup_{n=1}^{\infty}[\min_{\mathbf{k}\in Y^*}\kappa_n(\mathbf{k}),\max_{\mathbf{k}\in Y^*}\kappa_n(\mathbf{k})]. \qquad (25)$$

Such a spectrum is numerically computed in the next section and represented thanks to a so-called surface dispersion diagram in Fig. 1: Such a three-dimensional representation seems to be quite natural as we need two horizontal axes for the components of the Bloch vector k_1, k_2 which runs through the Brillouin zone Y^*, and one vertical axis for the wave frequency. For simplicity we only depict from herein two-dimensional diagrams (dispersion curves) assuming that

$$[\min_{\mathbf{k}\in Y^*}\kappa_n(\mathbf{k}),\max_{\mathbf{k}\in Y^*}\kappa_n(\mathbf{k})]=[\min_{\mathbf{k}\in \partial Y^*}\kappa_n(\mathbf{k}),\max_{\mathbf{k}\in \partial Y^*}\kappa_n(\mathbf{k})],$$

where ∂Y^* denotes the boundary of Y^*. In other words, we assume that to characterize completely the spectrum it is enough to describe merely the edges of the first Brillouin zone. We can see that this statement is indeed satisfied if we compare the surfaces of Fig. 1 with the continuous dispersion curves of Fig. 4 [note that we show only the reduced Brillouin zone ΓMX as depicted in Fig. 2(b), thanks to the fourfold symmetry of the structure]. Some simple proof can be found in the literature in the case of dilute inclusions, by considering a small perturbation in the plane-wave coefficients of Floquet-Bloch waves propagating within a homogeneous medium and noting that gaps are opening along the edges of Y^* due to degeneracy splits of the eigenstates [25]. But nonetheless, we are not aware of a more general mathematical proof for this result even in the case of convex inclusions of finite area fraction.

III. BAND DIAGRAMS AND NEGATIVE REFRACTION

We can now explore water waves undergoing negative refraction in a crystal that displays the all-angle negative refraction effect. The square array of rigid cylindrical fibers of square cross section is embedded within water. Our aim is to achieve some focusing effect of water waves using negative refraction, in a way similar to what was done for electromagnetism [8–10]. Our contribution compared with the numerical and experimental work on water waves of [19] is to provide an asymptotic model for the lensing effect in the case of densely packed square cylinders. We further compare approximate dispersion curves against that given by finite element computations when the inclusions come close to touching (plane-wave expansion method used in [19] is not well-suited in this case). We also give some numerical proof of lensing effect for a checkerboard water lens.

A. Analytical estimates for square cylinders with nearly touching edges

In this section we derive an asymptotic approximation of the potential within thin bridges Π_ε^j, $j=1,\ldots,4$, between close-to-touching square cylinders, as shown in Fig. 2. We will see that when ε tends to 0, the limit problem reduces to a one-dimensional Helmholtz equation. This equation is subject to boundary conditions set on a lattice. The idea underlying this analysis comes from an analogous model in continuum mechanics whereby one can approximate the acoustic vibrations of a phononic crystal consisting of a square array of close-to-touching voids by that of a lattice structure consisting of homogeneous strings of constant density [26].

Using local coordinates, we have

$$\Pi_\varepsilon^j=\{(x_1,x_2):a_j<x_1<b_j,|x_2|<\varepsilon h_j/2\}, \qquad (26)$$

where ε is a small nondimensional parameter, and a_j, b_j, and h_j are given constants denoting, respectively, the end points and thickness of the jth bridge. From (17) and (21), we know that the potential $\phi_j(x_1,x_2)$ satisfies the Helmholtz equation within Π_ε^j,

$$\nabla^2 \phi_j(x_1,x_2) + \kappa^2 \phi_j(x_1,x_2) = 0, \tag{27}$$

together with the homogeneous Neumann boundary conditions on the transverse boundaries

$$\left.\frac{\partial \phi_j}{\partial x_2}\right|_{x_2=\pm \varepsilon h_j/2} = 0. \tag{28}$$

This system can be supplied with appropriate boundary conditions at the ends of the bridge, namely for $x_1=a_j$ and $x_1=b_j$ (these conditions will be specified in the sequel).

Let us introduce the scaled variable

$$\xi = \frac{x_2}{\varepsilon}, \tag{29}$$

so that $\xi \in (-h_j/2,\ h_j/2)$ within Π_ε^j, and

$$\frac{\partial^2 \phi_j}{\partial x_2^2} = \frac{1}{\varepsilon^2}\frac{\partial^2 \phi_j}{\partial \xi^2}. \tag{30}$$

The rescaled Helmholtz equation in Π_1^j is

$$\left[\left(\frac{1}{\varepsilon^2}\frac{\partial^2}{\partial \xi^2} + \frac{\partial^2}{\partial x_1^2}\right) + \kappa^2\right]\phi_j = 0. \tag{31}$$

The potential ϕ_j is approximated in the form

$$\phi_j \sim \phi_j^{(0)}(x_1,\xi) + \varepsilon^2 \phi_j^{(1)}(x_1,\xi). \tag{32}$$

To leading order we obtain [see (28) and (31)]

$$\frac{\partial^2 \phi_j^{(0)}}{\partial \xi^2} = 0, \quad |\xi| < h_j/2, \tag{33}$$

$$\left.\frac{\partial \phi_j^{(0)}}{\partial \xi}\right|_{\xi=\pm h_j/2} = 0. \tag{34}$$

Hence, $\phi_j^{(0)} = \phi_j^{(0)}(x_1)$ (it is ξ independent). Assuming that $\phi_j^{(0)}$ is given, we derive that the function $\phi_j^{(1)}$ satisfies the following model problem on the scaled cross section of Π_1^j:

$$\frac{\partial^2 \phi_j^{(1)}}{\partial \xi^2} = -\frac{\partial^2 \phi_j^{(0)}}{\partial x_1^2} - \kappa^2 \phi_j^{(0)}, \quad |\xi| < h_j/2,$$

$$\left.\frac{\partial \phi_j^{(0)}}{\partial \xi}\right|_{\xi=\pm h_j/2} = 0. \tag{35}$$

The condition of solvability for the problem (35) has the form

$$\frac{d^2 \phi_j^{(0)}}{dx_1^2} + \kappa^2 \phi_j^{(0)} = 0, \quad a_j < x_1 < b_j. \tag{36}$$

Hence, we have shown that to the leading order we can approximate the potential ϕ within the thin bridge Π_ε^j by the function $\phi_j^{(0)}$ which satisfies the Helmholtz equation in one-space dimension (a harmonic oscillator).

Let us now assume that all bridges have the same thickness εh and length l and intersect orthogonally at nodes j as shown in Fig. 2(b). The Helmholtz equation (36) is now set in $(0,l)$ and if we denote Φ_j the potential at node j, (36) is supplied with the boundary conditions $\phi_j^{(0)}(0) = \phi(0,0) := \Phi_0$ and $\phi_1^{(0)}(l) = \phi(l,0) := \Phi_1$, $\phi_2^{(0)}(l) = \phi(0,l) := \Phi_2$, $\phi_3^{(0)}(l) = \phi(-l,0) := \Phi_3$, and $\phi_4^{(0)}(l) = \phi(0,-l) := \Phi_4$.

Considering first the case $\sin(\kappa l) \neq 0$, we obtain

$$\phi_j^{(0)}(x_1) = \Phi_0 \cos(\kappa x_1) + \frac{\Phi_j - \Phi_0 \cos(\kappa l)}{\sin(\kappa l)}\sin(\kappa x_1), \tag{37}$$

where κ is the spectral parameter satisfying the dispersion relation (15).

Equilibrium at the central node writes

$$0 = \sum_{j=1}^{4} \left.\frac{d^2 \phi_j^{(0)}}{dx_1^2}\right|_{x_1=0}$$

$$= \frac{1}{\sin(\kappa l)}[\Phi_1 + \Phi_2 + \Phi_3 + \Phi_4 - 4\Phi_0 \cos(\kappa l)]. \tag{38}$$

Note that the same holds true for the displacement of the node in the plane perpendicular to a lattice of homogeneous strings of constant density [26].

The Floquet-Bloch condition leads to

$$\Phi_1 = e^{-ik_1 l}\Phi_0, \quad \Phi_2 = e^{-ik_2 l}\Phi_0,$$

$$\Phi_3 = e^{ik_1 l}\Phi_0, \quad \Phi_4 = e^{ik_2 l}\Phi_0, \tag{39}$$

where $\mathbf{k} = (k_1,k_2)$ is the Bloch vector.

Substituting the quasiperiodicity conditions (39) and (38), we finally obtain

$$\cos(k_1 l) + \cos(k_2 l) - 2\cos(\kappa l) = 0. \tag{40}$$

For the case $\sin(\kappa l) = 0$, there exists, for any $\mathbf{k}$, standing wave modes corresponding to internal vibrations of bridges, with no displacement at the nodes.

Altogether, the dispersion relation in thin-bridges writes

$$\sin(\kappa l)[\cos(k_1 l) + \cos(k_2 l) - 2\cos(\kappa l)] = 0. \tag{41}$$

We note that this dispersion relation was also obtained in [26] for an analogous problem of harmonic vibrations of a lattice of strings, as discussed above.

For a wave propagating in the ΓX direction, $k_1 = k_2$, so that (41) reduces to $\kappa = k_1$. This has important practical consequences as it gives the frequency at which focusing of water waves occurs for a slab lens consisting of close to touching square cylinders.

B. Analysis of band diagrams

To analyze the transport of water-wave energy within the array of cylinders, we need to link the dispersion relation to that of propagation of energy. This can be done in a way similar to what was discussed for electromagnetism in [9].

First, we note that the group velocity of Floquet-Bloch water waves is defined as [27]

$$\mathbf{V}_g = \nabla_{\mathbf{k}}(\omega) = \frac{\partial \omega}{\partial k_1}\mathbf{e}_1 + \frac{\partial \omega}{\partial k_2}\mathbf{e}_2. \tag{42}$$

Note that this group velocity corresponds to the speed at which the amplitude of the envelope of the water wave

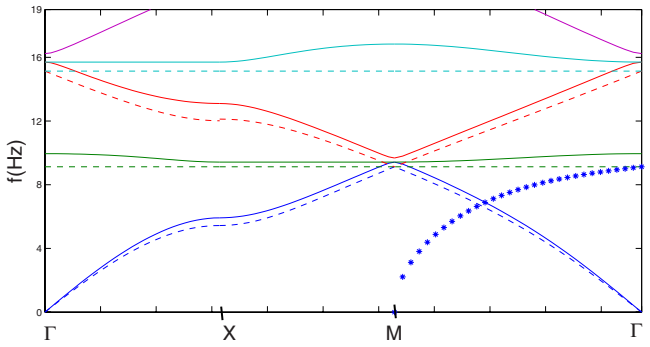

FIG. 5. (Color online) Same as Fig. 4 but for a filling fraction of cylinder in water of 0.7.

propagates, whereas the phase speed propagates with the speed of, say, the crest of the waves. The group velocity is easily seen to be equal to the average velocity (taken over the basic cell) of the energy flow.

Second, we note that the phase velocity V_ϕ of water waves measures the phase difference ϕ, i.e., a time delay, between the motion of two particles on the free surface ξ. The wavelength is the distance between two particles whose motion have the same phase. Note that acoustic waves propagating within a compressible medium have a velocity independent of wavelength (no dispersion), unlike surface water waves. We further note that surface water waves propagating in deep water propagate with a phase velocity which increases with wavelength, similar to the phase velocity of light (which actually behaves as the inverse of the refractive index). This is easily seen by taking h tend to infinity in (15). On the contrary, surface water waves in shallow water ($h \ll 1$ which is our case) behave the other way around.

The essential condition for the all-angle-negative refraction (AANR) effect is that the equifrequency surfaces (EFS) should become convex everywhere about some point in the reciprocal space, and the size of this EFS should shrink with increasing frequency. Further the EFS should be larger than the free space dispersion surface and the frequency should be within the first Bragg zone [8–10].

In order to understand how we will choose the working frequency let us recall some basic elements. We consider a slab of crystal, i.e., a crystal finite along one direction and infinite along the two others. The reasoning is based on the fact that due to the periodicity of the structure the tangential component of the incident wave vector should be conserved, that is to say that the tangential components of the excited Bloch waves and the incident wave should be equal. The interested reader can find a more detailed analysis of the last point in [9]. The graphical representation in Fig. 3 may help understand how the negative refraction occurs. The circle centered on Γ represents the EFS of the waves propagating freely on the water surface without any inclusion, while the circle centered on the Γ points stands for the EFS for the Bloch waves propagating in the crystal. Note that this is an idealized sketch as the EFS of the Bloch mode are usually of more complex shape. We consider an incident plane wave whose wave vector is represented by the arrow starting from Γ. We assume that the interface of the crystal is perpendicular to the direction Γ-M, thus the Bloch waves that could be excited are given by the intersection between the dashed lines and the EFS of the Bloch waves in the crystal (conservation of the tangential component of the wave vector). The propagation of the energy of the Bloch wave is given by the normal to the EFS and directed toward the ascending side of the band. Thus if the EFS shrinks around the point M when the frequency increases one obtains a negative refraction as

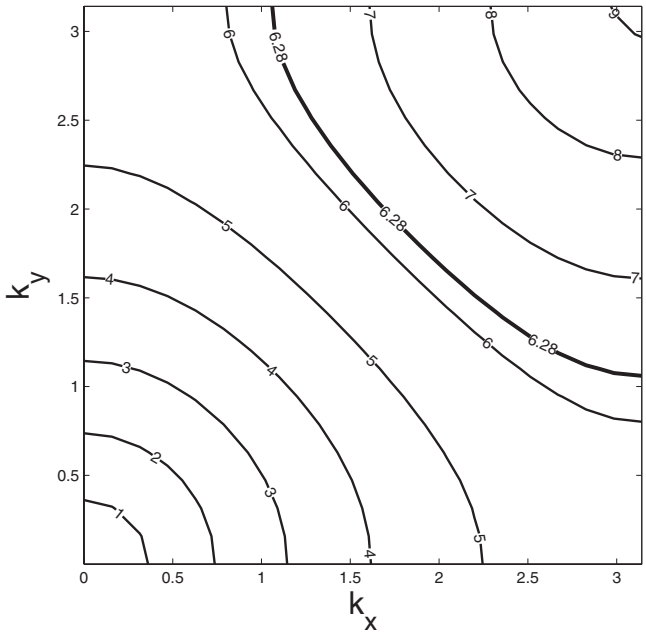

FIG. 6. Isofrequencies corresponding to dispersion curves of Fig. 4.

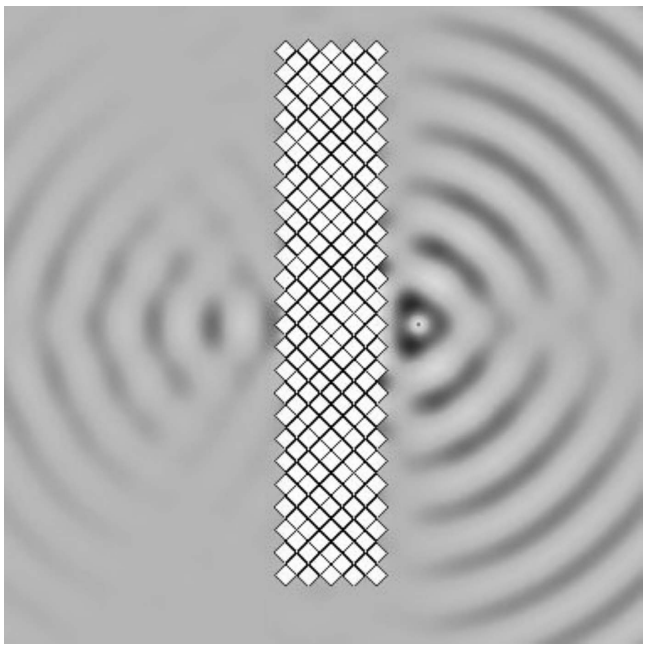

FIG. 7. Water-wave lensing for one source at frequency $f_{\text{lens }1} = 6.28 \sim 2\pi$ Hz, through an array of 212 square cylinders of side length 9.5 mm. The pitch of the array is 10 mm, the depth of water is $h=6$ mm, and the capillarity $d_c=0.109$ mm.

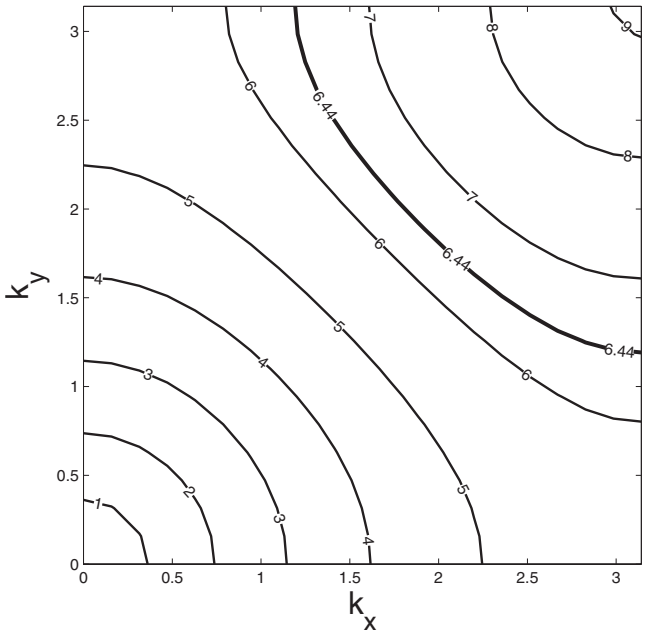

FIG. 8. Isofrequencies corresponding to dispersion curves of Fig. 5.

shown by the two arrows on the right-hand part of Fig. 3. Note that the two solutions exists in the slab but in a semi-infinite crystal an outgoing wave condition would allows us to eliminate the Bloch mode corresponding to the left-most arrow.

As can be seen in Fig. 4, the analytical formula (41) compares very well with the finite elements computations for a filling fraction of 0.9. The larger the filling fraction, the better the approximation, as is obvious from Fig. 5. We note that for a filling fraction of 1, we are left with only water so that the dispersion relation reduces to that of surface waves propagating at the interface between water and air. The starred curve in Fig. 4 corresponds to this case for a depth of water of $h=6$ mm. Its intersection with the acoustic band provides us with the frequency at which negative refraction occurs. We note that this frequency is around $f_{\text{lens }1}=2\pi$ Hz, which is a straightforward consequence of (15) and (41). We check in Fig. 6 that the corresponding EFS satisfy the criteria for AANR and we indeed observe on Fig. 7 that for a harmonic source set at this frequency, there is indeed an image forming on the other side of the array.

It is remarkable that a water-wave image occurs for such a densely packed array of cylinders. In the thin bridges between the cylinders, the potential is given analytically by (37). We also note that boundary layers may occur on the walls of the thin channels as already analyzed in [20,28] for magnetohydrodynamics, hence the water profile is flattened in the thin channels, which may result in slow surface waves. But after an intermediate regime, negative refraction will take place anyway, and an image will eventually form on the other side of the lens.

For a filling fraction of 0.5, the corresponding equifrequencies and the numerical evidence of super-lensing are shown in Figs. 8 and 9, where the source is now set a the frequency $f_{\text{lens }2}=6.44$ Hz. In this case, there is more space

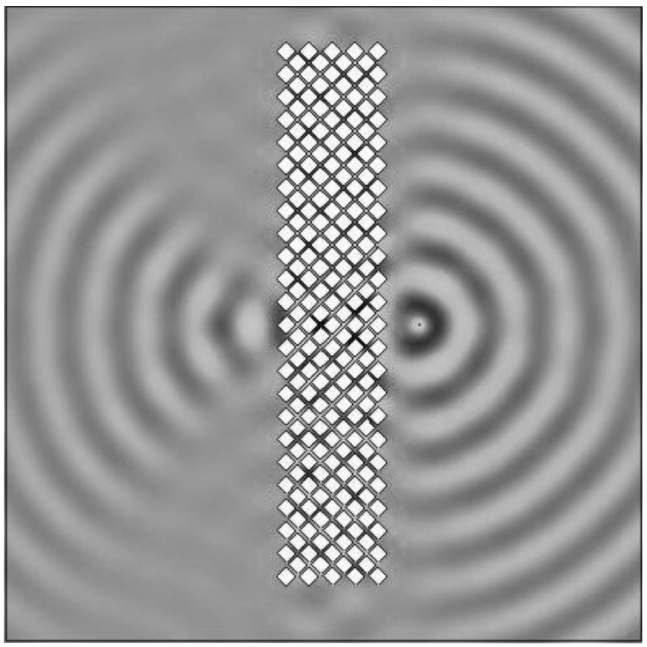

FIG. 9. Water-wave lensing for one source at frequency $f_{\text{lens }2}=6.44$ Hz, through an array of 212 square cylinders of side length 8.4 mm. The pitch of the array is 10 mm, the depth of water is $h=6$ mm and the capillarity $d_c=0.109$ mm.

for the water to flow between cylinders, hence the image is more apparent. In Fig. 10, we numerically show, using two sources set at the same frequency $f_{\text{lens }2}$, that the flat lens exhibits no astigmatism, as was predicted by Veselago long ago for a slab of negative refractive index $n=-1$ [1].

We now report in Fig. 11 the evolution of the width of the first partial gap along the ΓM direction against the filling

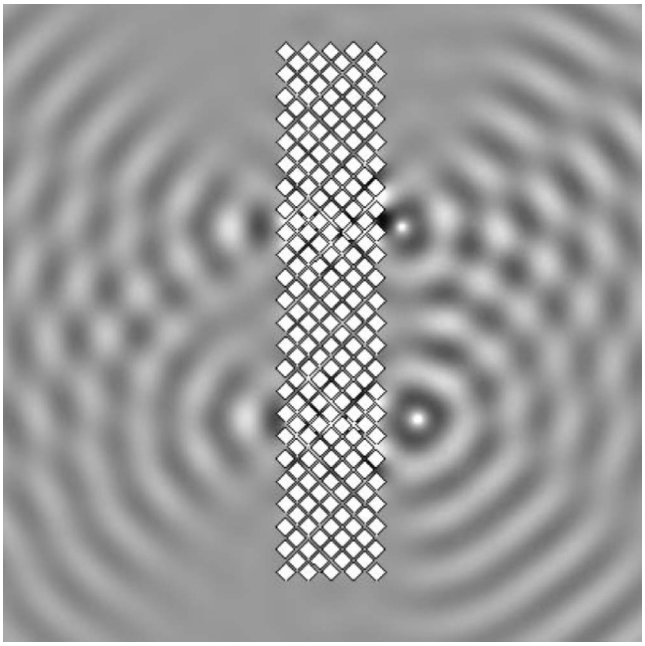

FIG. 10. Water-wave lensing for two sources at frequency $f_{\text{lens }2}=6.44$ Hz through the same array as in Fig. 9. The slab lens exhibits no astigmatism, since its effective refractive index is −1.

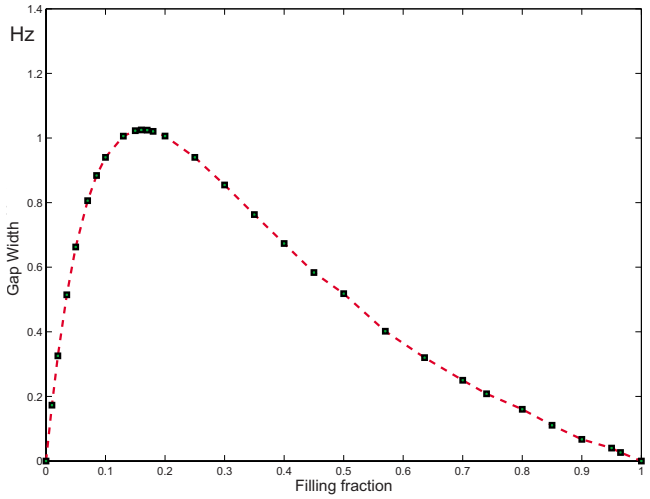

FIG. 11. (Color online) Evolution of the width of the partial gap (in Hz) along the ΓM direction, with respect to the filling fraction F of the square inclusion in the unit cell.

fraction of cylinder in the basic cell. As can be expected, the width of the gap vanishes in the limit cases of dilute and densely packed cylinders: For both limit cases $F=0$ and $F=1$, the cylinders are no longer present and water flows freely. Interestingly, the curve reaches its maximum around a filling fraction $F=0.16$ for which there is no obvious explanation.

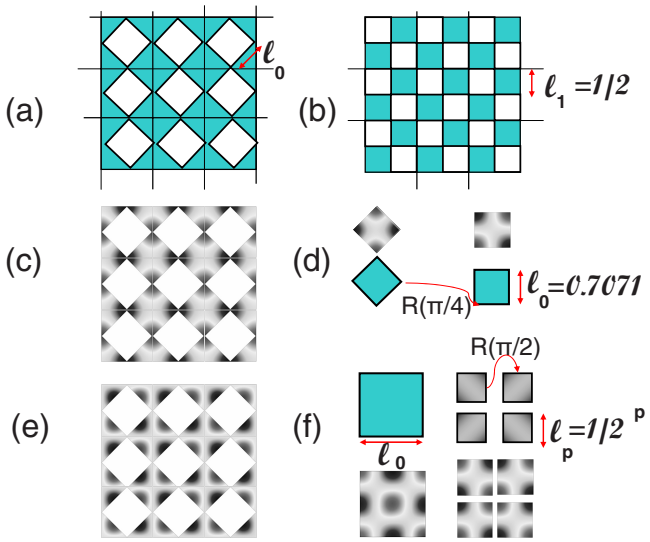

FIG. 12. (Color online) (a) Square array of pitch 1 of square cylinders of side length $l_0=0.7071$ mm which make an angle $\pi/2$ with the lattice vectors (the blue region is filled with water). (b) Same array now filled with nonrotated square cylinders of side length $l_p=1/2^p$. (c) Typical eigenmode (of say, type I) associated with the square array in (a). (d) Water tank of side length l_0 whose frequencies approximate that of localized modes of (c). (e) Typical eigenmode (of say, type II) associated with the square array in (a). (f) Left: water tank of side length l_0 whose resonant frequencies approximate that of localized modes of the chessboard in (b). Right: reconstruction of an eigenmode of cavity of side length l_0 (left panel) through $\pi/2$ rotation of an eigenmode of cavity of side lenth l_p; this eigenmode is also recovered from a $\pi/4$ rotation of the localized mode in (d): Localized eigenmodes are self-similar in chessboards, up to a $\pi/4$ rotation.

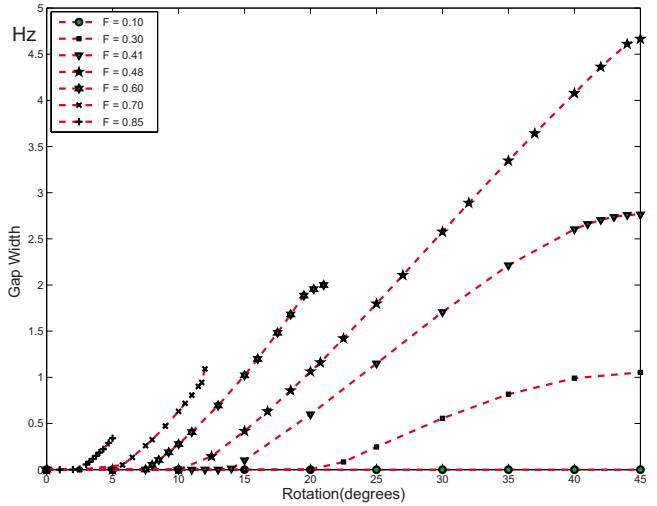

FIG. 13. (Color online) Evolution of the width of the full gap (in Hz), with respect to the rotation (in degrees) of the cylinders within the array. Each curve corresponds to a given filling fraction F of the square inclusion in the unit cell. We note that above 0.48 the rotation cannot exceed a given value, hence the curve stops at this angle.

C. Water waves in checkerboards

Let us now rotate the square cylinders within the square array. (See Figs. 12–16.) We report in Fig. 13 the evolution of the width of the first complete gap with respect to the angle of rotation. Not surprisingly, the curve reaches its maximum for a rotation of $\pi/4$, whenever the inclusion is allowed to rotate through such an angle: This is a consequence of the fourfold symmetry of the inclusion and the array. But when the inclusion becomes too large (its filling

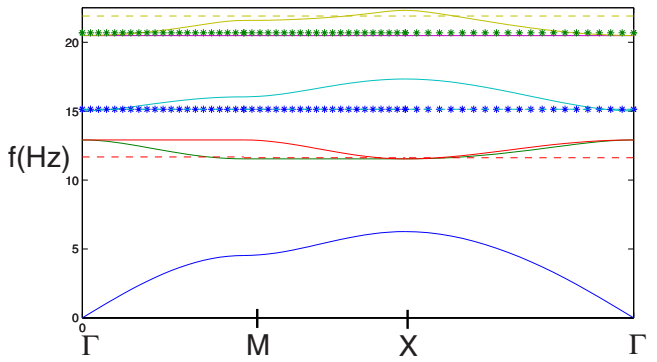

FIG. 14. (Color online) FEM computations of dispersion curves (continuous curves) for a checkerboard consisting of a square array of square cylinders in water for a filling fraction 0.49, when rotated by an angle $\pi/2$. Horizontal axis: Projection of the Bloch vector on the first Brillouin zone ΓXM. Vertical axis: Wave frequency $f=\omega/(2\pi)$ in Hz. The dotted and starred curves, respectively, stand for the first three frequencies of water tanks of length $l_0=0.7071$ mm and $l_1=0.5$ mm. The depth of water is $h=6$ mm and the capillarity $d_c=0.109$ mm.

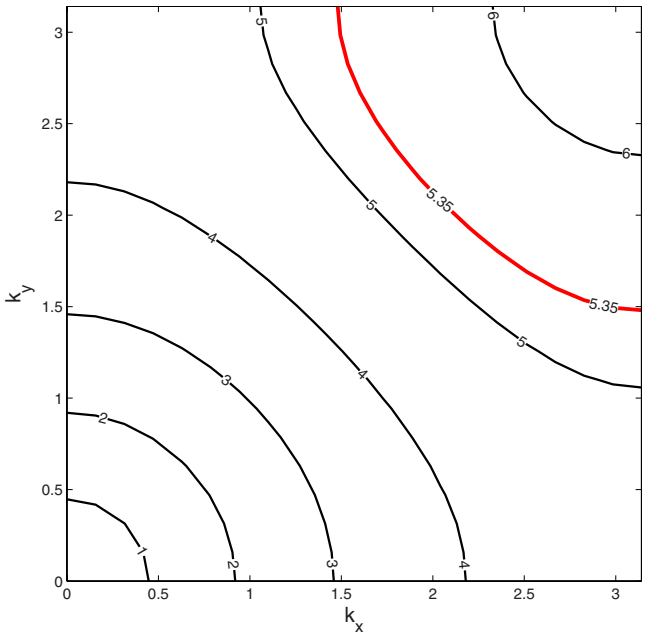

FIG. 15. (Color online) Isofrequencies corresponding to dispersion curves of Fig. 14.

fraction goes over $F=0.5$), the curve remains monotonic but it ends for a rotation angle which is the last admissible one. We also note that the higher the filling fraction, the steeper the slope of the curve. To enlarge the gap the best we can, while keeping enough space for water to flow between cylinders, we therefore choose a filling fraction of $F=0.49$ and a rotation angle of $\pi/4$. In this way, we generate a checkerboard consisting of water (white cells) and square cylinders (black cells). Such structure, which bears some resemblance with that studied, has also some possible connection with the Babinet principle, which says that for an infinitely thin checkerboard lit from above in the subwavelength regime, transmission and reflection are perfectly balanced (they are both equal to one-half), as discussed in [29]. Nevertheless, in our case the water rather flows in the transverse direction, but we can clearly see from Fig. 16 that the lensing effect is partly spoiled by reflections on the interface between the checkerboard lens with free water, even though the source is set at a frequency $f_{\text{checkerlens}}=5.35$ Hz for which negative refraction occurs, as deduced from the dispersion curve in Fig. 14 and the corresponding equifrequencies in Fig. 15. It could be that only one-half of the waves are transmitted and hence contribute toward the image.

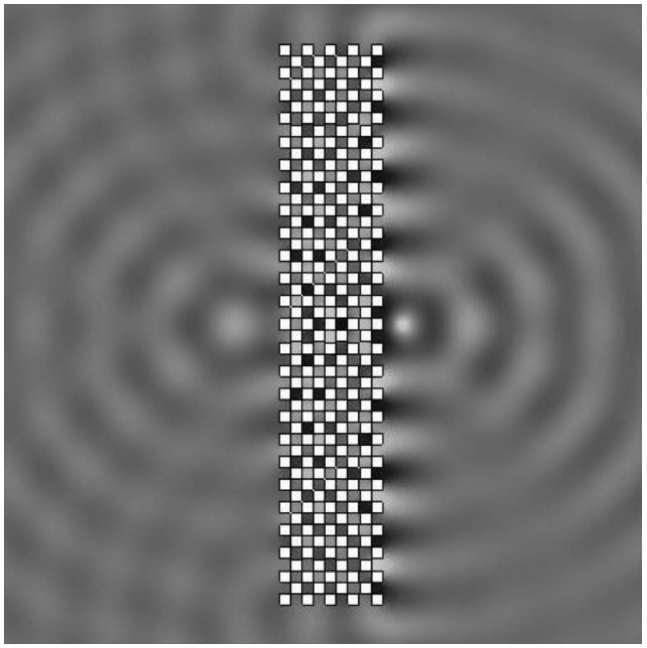

FIG. 16. Water-wave lensing for a source set at a frequency 5.35 Hz through an array of 212 square cylinders of side length 8.4 mm which are rotated by $\pi/2$. The pitch of the array is 10 mm.

D. Analytical estimates for square cylinders with nearly touching vertices

Let us also note that some of the dispersion curves in Fig. 14 are reasonably approximated by resonances for a square water tank. In this case, the reduced potential ϕ satisfies the Helmholtz equation (17) in a square domain $\Sigma=(0,l)^2$ and it is supplied with Neumann boundary conditions on its boundary $\partial\Sigma$. Looking for nontrivial eigenfields ϕ of finite energy in Σ, the resolvent of the operator associated with this spectral problem is compact, hence its spectrum consists of a countable set of positive eigenvalues. Using separation of variables, these eigenvalues κ straightforwardly satisfy

$$\kappa=\frac{\pi}{l}\sqrt{n^2+m^2},\quad (n,m)\in\mathbb{N}^2\setminus\{(0,0)\},\tag{43}$$

and their associated eigenfield is written as

$$\phi(x_1,x_2)=\phi_0\cos\left(\frac{n\pi}{l}x_1\right)\cos\left(\frac{m\pi}{l}x_2\right),\tag{44}$$

where ϕ_0 is a constant field. Taking $l=0.7071$ in (43), we can see that the first eigenvalue $\kappa_0^{(1)}=\pi/0.7071$ and the next two ones are $\kappa_0^{(2)}=\pi\sqrt{2}/0.7071$ and $\kappa_0^{(3)}=\pi\sqrt{4}/0.7071$. Assuming that the length l is in millimeters, this in turns gives us the water waves frequencies $f_0^{(1)}=11.62$ Hz, $f_0^{(2)}=15.13$ Hz, and $f_0^{(3)}=20.69$ Hz. These frequencies are reported as horizontal dotted lines in Fig. 14. One can see that $f^{(1)}$ corresponds to the second and third dispersion curves [indeed this eigenfrequency has a degeneracy of order 2 since it corresponds to pairs $(m_0,n_0)\in\{(0,1),(1,0)\}$]. We note that it gives an accurate estimate for the upper edge of the first gap lying within the frequency range [6.5 Hz, 11.5 Hz]. The next eigenfrequency $f^{(2)}$ is a reasonable approximation for the frequency of the (nondegenerated) trapped mode sitting inside the second gap in the frequency range [13 Hz, 20.5 Hz]. As for $f^{(3)}$ it provides a reasonable approximation for the eigenfrequency of the localized mode sitting right on the upper edge of the second gap. We numerically checked that the next frequencies of the water tank of side length $l_0=0.7071$ mm provide us with the location of the next gaps and trapped modes (with one trapped mode per gap). Nevertheless, we were not able to catch up with the lower edge of

the very first gap since we did not find an accurate estimate for the acoustic band (the first dispersion curve).

We numerically observe that frequencies of localized modes of the checkerboard lens are well approximated not only by that of a water tank of side length $l_0=0.7071$ mm but also by that of a water tank of side length $l_1=0.5$ mm (from now on we drop the unit of length for the sake of simplicity, assuming that all lengths are in millimeters for the applications we have in mind). Indeed, when we compare the corresponding dotted and starred horizontal lines in Fig. 14, we can see that they are fairly close to each other. It is even apparent from the diagram in Fig. 14 that the second eigenfrequency of the water tank of side length l_1 provides a better approximation of the fourth dispersion curve. We nonetheless note that the first localized eigenfrequency is not caught by that water tank. It is actually obvious from (43) that water tanks of side length $l_p=1/2^p$, where p is a strictly positive integer, will never catch up to that frequency.

We will show in the sequel that except for this fundamental mode of the cavity of side length $l_0=0.7071$ mm, any other mode will have its counterpart in a water tank of side length $l_p=1/2^p$. We note that all of these water tanks can be considered as building blocks of an infinite checkerboard whose filling fraction of cylinders in water is obviously one-half (see Fig. 12): Such a structure is self-similar under a scaling of one-half, hence any square cell of side length l_p such that $l_p=1/2^p$ gives rise to a checkerboard which is isomorphic to the checkerboard with a square cell of side length $l_0=0.7071$ mm, as transpires from Figs. 12(a)–12(f).

This suggests that we should be able to establish that the spectrum σ_0 of the checkerboard with cells of side length l_0 can be identified with the union of the spectra σ_p of all checkerboards with cells of side length $l_p=1/2^p$ and side length $\sqrt{2}l_p=1/2^{p-1/2}$:

$$\sigma_0 = \bigcup_{p=1}^{\infty} \{\sigma_p \cup \sqrt{2}\sigma_p\}. \tag{45}$$

Such result bears some resemblance with Keller's theorem for effective properties of high contrast checkerboards [30].

In the present case, the statement comes down to show that there always exists an integer $p \geq 1$ such that

$$\kappa_p = \kappa_0 \quad \text{or} \quad \sqrt{2}\kappa_p = \kappa_0, \tag{46}$$

where κ_p and κ_0 are eigenvalues, respectively, for the cavities of side lengths $1/2^p$ and $l_0 \sim 0.7071$. From (43), this means the following arithmetic constraint should be satisfied for a given $p \in \mathbb{N}\backslash\{0\}$:

$$\frac{1}{2^{2p-1}} = \frac{l_p^2}{l_0^2} = \frac{n_p^2+m_p^2}{n_0^2+m_0^2}, \tag{47}$$

where $(m_0,\ m_p,\ n_0,\ n_p) \in \mathbb{N}^4\backslash\{(0,0,0,0)\}$. We first note that when p is large, $n_0^2+m_0^2$ should be much larger than $n_p^2+m_p^2$. Furthermore, $n_0^2+m_0^2$ should be an even number. Hence, finding integers satisfying the constraint (47) is not trivial.

For the sake of illustration, let us look at the first few possible solutions. For instance, taking $p=1$ in (47), we should find $(m_0,\ m_1,\ n_0,\ n_1) \in \mathbb{N}^4\backslash\{(0,0,0,0)\}$ such that

$$n_0^2+m_0^2 = 2(n_1^2+m_1^2). \tag{48}$$

Clearly, there exists no pair (m_1,n_1) such that (48) is satisfied for $(m_0,n_0) \in \{(0,1),(0,3),(1,0),(1,2),(2,1),(2,3),(3,2)\}$. On the contrary, there exist (nonunique) pairs $(m_1,n_1) \in \mathbb{N}^2$ such that (48) is satisfied for $(m_0,n_0) \in \{(0,2),(1,1),(1,3),(2,0),(2,2),(3,0),(3,1),(3,3)\}$. Hence, one can see that it is not enough to consider $p=1$ in (47) to recover all pairs of integers (m_0,n_0) associated with the spectrum σ_0 from the pairs (m_p,n_p) associated with the spectrum σ_p. As suggested by the above discussion, identifying σ_0 with σ_p involves a lacunary process. Giving fine estimates for the distribution of integers $m_0,\ n_0, m_p,\ n_p$ satisfying (47) is a task which falls into the topic of number theory.

But for the present analysis it is enough to note that we are ensured of the existence of pairs of integers (n_0,m_0), (n_p,m_p) satisfying (47) for a given integer $p \geq 1$, since only squares of integers are involved on the right-hand side of (47) and also since 1/2 is a (not continuous) fraction [31]. Summing over p in both sides of (47), we thus obtain

$$\sum_{p=1}^{\infty} (n_p^2+m_p^2) = \frac{2}{3}(n_0^2+m_0^2), \tag{49}$$

since the sum $\Sigma_{p=1}^{\infty} l_p^2/l_0^2 = \Sigma_{p=1}^{\infty} 1/2^{2p-1} = 2/3$. Noting that $\Sigma_{p=2}^{\infty} 1/2^{2p-2} = 1/3$ puts an end to the proof of the proposition (45).

Let us recall that (45) is linked with Keller's theorem for effective properties of high contrast checkerboards. Interestingly, Keller's result holds true for more complex geometries satisfying some mirror symmetry. It was generalized by Dykhne [32] to checkerboards of finite conductivities σ_1 and σ_2 (the effective conductivity is then given by $\sqrt{\sigma_1\sigma_2}$), and also to two-dimensional isotropic polycrystals. These results were further extended to complementary media described by heterogeneous anisotropic matrices of permittivity for the case of dynamic effective properties in electromagnetism [33]. Not surprisingly, in this last case the effective properties are no longer given in closed form but are deduced from auxiliary problems of electrostatic type. Such results imply that if a microstructure is not isotropic but is such that interchanging the phases produces the same effect as rotating the structure by $\pi/2$, then the effective properties are isotropic and the effective refractive index is unchanged. Interestingly, Craster and Obnosov succeeded in getting effective properties of four phase checkerboards in closed form in the context of conductivity [34]. Last, Babinet's principle may well still apply for such complex media [29]. Therefore, there is room here for much more work on focusing effect for water waves through complex structured (multiphases) lenses satisfying certain mirror symmetries.

IV. CONCLUSION

We emphasize that our analysis encompasses also the important case of electromagnetic waves propagating in square arrays of infinite conducting square cylinders, in *s* polarization (the Neumann boundary condition is a good approxima-

tion for infinite conducting walls in the microwave regime). For this, one simply must take $\kappa=\omega\sqrt{\varepsilon_r}/c$, where ε_r is the relative permittivity of the matrix (equal to one for vacuum) and c is the speed of light in vacuum. It also covers the case of antiplane shear acoustic waves propagating through a square array of square voids if we take $\kappa=\omega\sqrt{\rho/\mu}$ where ρ and μ are, respectively, the density and shear modulus of the matrix material. In this case, the Neumann boundary condition describes traction free bodies and the sound speed is $c=\sqrt{\mu/\rho}$. For potential applications in tomography, we would be looking for ultrasonic waves for instance. In a way similar to the parallel drawn in [3] between Alice's mirror and Pendry's perfect lens, we may push the parallel further between our checkerboard lens and Alice's checkerboard where the white queen remembers events yet to come (from the future): If evanescent waves are enhanced in some way, the checkerboard lens may open a Pandora's box containing some acoustic, electromagnetic or hydrodynamic paradigms depending upon the study. Potential applications range from flat water lenses (counterpart of the Pendry-Veselago lens in electromagnetism) to localization of water-wave energy (cf. cloaking effect for a source radiating in the neighborhood of a photonic crystal slab lens when AANR occurs).

ACKNOWLEDGMENTS

The authors (M.F., S.G., S.E., and G.T.) acknowledge the EC funded project PHOREMOST under Grant No. FP6/2003/IST/2-511616. This work was partly supported by the research program METAPHORE (AC Nanosciences and Nanotechnologies of the *French Ministère de la Recherche et des Nouvelles Technologies*). The authors (S.G., A.B.M., and N.V.M.) are thankful for the Franco-British Partnership Programme ALLIANCE (Contract No. PN 05.026).

[1] V. G. Veselago, Usp. Fiz. Nauk **92**, 517 (1967); V. G. Veselago, Sov. Phys. Usp. **10**, 509 (1968).
[2] J. B. Pendry, Phys. Rev. Lett. **85**, 3966 (2000).
[3] D. Maystre and S. Enoch, J. Opt. Soc. Am. **21**, 122 (2004).
[4] S. Guenneau, A. C. Vutha, and S. A. Ramakrishna, New J. Phys. **7**, 164 (2005).
[5] D. R. Smith, W. J. Padilla, D. C. Vier, S. C. Nemat-Nasser, and S. Schultz, Phys. Rev. Lett. **84**, 4184 (2000).
[6] S. A. Ramakrishna, Rep. Prog. Phys. **68**, 449 (2005).
[7] E. Yablonovitch, Phys. Rev. Lett. **58**, 2059 (1987).
[8] R. Zengerle, J. Mod. Opt. **34**, 1589 (1987).
[9] B. Gralak, S. Enoch, and G. Tayeb, J. Opt. Soc. Am. A **17**, 1012 (2000).
[10] M. Notomi, Opt. Quantum Electron. **34**, 133 (2002).
[11] C. Luo, S. G. Johnson, J. D. Joannopoulos, and J. B. Pendry, Phys. Rev. B **65**, 201104(R) (2002).
[12] X. Zhang and Z. Liu, Appl. Phys. Lett. **85**, 341 (2004).
[13] X. Hu, Y. Shu, X. Liu, R. Fu, and J. Zi, Phys. Rev. E **69**, 030201(R) (2004).
[14] L. Feng, X. P. Liu, M. H. Lu, Y. B. Chen, Y. F. Chen, Y. W. Mao, J. Zi, Y. Y. Zhu, S. N. Zhu, and N. B. Ming, Phys. Rev. B **73**, 193101 (2006).
[15] T. Chou, Phys. Rev. Lett. **79**, 4802 (1997).
[16] T. Chou, J. Fluid Mech. **369**, 333 (1998).
[17] P. McIver, J. Fluid Mech. **424**, 101 (2000).
[18] M. Torres, J. P. Adrados, F. R. Montero de Espinosa, D. Garcia-Pablos, and J. Fayos, Phys. Rev. E **63**, 011204 (2000).
[19] X. Hu, Y. Shen, X. Liu, R. Fu, J. Zi, X. Jiang, and S. Feng, Phys. Rev. E **68**, 037301 (2003).
[20] L. D. Landau, E. M. Lifschitz, and L. P. Pitaevskii, *Electrodynamics of Continuous Media* (Butterworth-Heinemann, New York, 1984).
[21] N. Kuznetsov, V. Maz'ya, and B. Vainberg, *Linear Water Waves: A Mathematical Approach* (Cambridge University Press, Cambridge, England, 2002).
[22] A. Nicolet, S. Guenneau, C. Geuzaine, and F. Zolla, J. Comput. Appl. Math. **168**, 321 (2004).
[23] www.comsol.com
[24] C. Conca, J. Planchard, and M. Vaninnathan, *Fluids and Periodic Structures, RAM: Research in Applied Mathematics* (Wiley, New York, 1995), Vol. 38.
[25] C. Kittel, *Introduction to Solid State Physics*, 8th ed. (Wiley, New York, 2005).
[26] P. G. Martinsson and A. B. Movchan, Q. J. Mech. Appl. Math. **56**, 45 (2003).
[27] P. Yeh, J. Opt. Soc. Am. **69**, 742 (1979).
[28] S. Guenneau, A. B. Movchan, C. G. Poulton, and A. Nicolet, Q. J. Mech. Appl. Math. **57**, 407 (2004).
[29] R. C. Compton, J. C. Macfarlane, L. B. Whitbourn, M. M. Blanco, and R. C. McPhedran, Opt. Acta **31**, 515 (1984).
[30] J. B. Keller, J. Appl. Phys. **34**, 991 (1963).
[31] G. H. Hardy and E. M. Wright, *An Introduction to the Theory of Numbers* (Oxford University Press, Oxford, England, 1980).
[32] A. M. Dykhne, Sov. Phys. JETP **32**, 63 (1971).
[33] F. Zolla and S. Guenneau, Phys. Rev. E **67**, 026610 (2003).
[34] R. V. Craster and Y. V. Obnosov, SIAM J. Appl. Math. **61**, 1839 (2001).